Rothamsted Repository Download

A - Papers appearing in refereed journals

Wang, D., Gao, Y., Li, M., Sturrock, C. J., Gregory, A. S. and Zhang, X. 2020. Change in hydraulic properties of the rhizosphere of maize under different abiotic stresses . *Plant and Soil.*

Change in hydraulic properties of the rhizosphere of maize under different abiotic stresses

Di Wang[1,3], Yang Gao[2*], Ming Li[3], Craig J. Sturrock[4], Andrew S. Gregory[1], Xiaoxian Zhang[1,]

[1] Department of Sustainable Agricultural Sciences, Rothamsted Research, Harpenden, Hertfordshire, AL5 1GQ, UK

[2] Institute of Farmland Irrigation, Chinese Academy of Agricultural Sciences, Xinxiang, 453002, Henan Province, P.R. China

[3] School of Engineering, University of Liverpool, Brownlow Street, Liverpool L36 1GQ, UK.

[4] Division of Agricultural and Environmental Sciences, University of Nottingham, Sutton Bonington Campus, Loughborough, Leicestershire, LE12 5RD, UK

* Authors to whom correspondence should be addressed

Abstract

Background and aims: Root growth alters the rhizosphere thereby affecting root uptake of water and nutrients. However, the influence of abiotic stress on this process is poorly understood. In this study we investigated the effects of water and salinity stresses (both in isolation and combined) on maize (*Zea mays* L.).

Methods: Seedlings were grown in pots packed with a loamy sand soil for two weeks and then subjected to water and salinity stresses, together with an unstressed control. After an additional two weeks, plants were removed from the pots and the soil aggregates adhering to the roots were collected and scanned using X-ray Computed Tomography. The ability of the aggregates to conduct water was calculated from pore-scale simulation of water flow using the lattice Boltzmann method.

Results: It was found that both water and salinity stresses reduced the permeability of the rhizospheric aggregates, although the reduction under salinity stress was more significant than under water stress. Combining water and salinity stresses reduced the permeability of the rhizosphere by one order in magnitude compared to the unstressed rhizosphere.

Conclusions: Abiotic stresses work with root-induced activity to reshape the rhizosphere. As water and nutrients need to pass through the rhizosphere before being taken up by roots, understanding such rhizosphere changes has an important implication in plant acquisition of soil resources.

Key words: *Rhizospheric permeability; pore-scale modelling; abiotic stress; tortuosity.*

1. Introduction

The rhizosphere is the small volume of soil impacting and being impacted on by plant roots. It is the most active zone in terrestrial ecosystem (Gregory 2006). The large quantity of rhizodeposits secreted by roots, along with the imbalanced uptake of cations and anions by roots, makes the rhizosphere differ markedly from the bulk soil both physically and biochemically (Hinsinger et al. 2005). Early experiments showed that root growth led to a densification of the rhizosphere (Dexter 1987), while recent studies found that root-mediated physical and biological processes could also increase the rhizosphere porosity through enhancing aggregation (Helliwell et al. 2019; Rabbi et al. 2018).

The change in physical properties of the rhizosphere is a result of the interplay of a multitude of biotic and abiotic processes (Hinsinger et al. 2009). Physically, root growth radically deforms adjacent soil resulting in a compression of the surrounding pore space. In contrast, mucilage and extracellular polysaccharides (EPS) exuded by roots and microorganisms have been shown to boost soil aggregation and increase the number of large pores relevant to water and nutrient flow (Alami et al. 2000). In addition to restructuring the rhizosphere, the mucilage and EPS also alter the surface tension and viscosity of soil water (Ahmed et al. 2018; Carminati 2012; 2013; Hallett et al. 2003; Read et al. 2003; Read and Gregory 1997; Zarebanadkouki et al. 2016), rendering the rhizosphere either hydrophilic or hydrophobic depending on its moisture content (Carminati et al. 2010; Carminati et al. 2011). Such a dynamic change in physical properties of the rhizosphere has a paramount impact on root uptake of water and nutrients (Kroener et al. 2014; Schwartz et al. 2016).

Most research on change in the rhizosphere hydraulic properties has focused on water retention, whereas there is a paucity of studies on alteration of the rhizospheric hydraulic conductivity as directly measuring water flow in the rhizosphere is very difficult even using modern tomography (Huang et al. 2015; Ren et al. 2015) and tracer- based technologies

(Totzke et al. 2017). As a result, indirect methods have been used as an approximation. For example, Zarebanadkouki et al. (2016) calculated the permeability of a lupin rhizosphere based on radiographic images acquired using neutron tomography, and Rabbi et al (2018) calculated the permeability of a chickpea rhizosphere through pore-scale simulation based on X-ray CT images. Similar methods had also been used by others to calculate the unsaturated hydraulic conductivity of the rhizosphere (Daly et al. 2015; Tracy et al. 2015). These indirect methods provided some insight into how roots modulate their rhizosphere to facilitate water uptake, but they need to make assumptions about water flow in the void space which are difficult to justify experimentally. For example, the pore-scale simulations need to know the water velocity at the water-solid and water-air interfaces. While the water-solid interface could be assumed to be a non-slip boundary in hydrophilic soil where the water velocity is zero (Rabbi et al. 2018), the water-air interface for unsaturated flow is difficult to decide *a priori* (Tracy et al. 2015; Zhang et al. 2016c). Research on using neutron imaging to inversely estimate the hydraulic conductivity of the rhizosphere has shown potential, but it required information on hydraulic conductance of the roots which is difficult to measure *in vivo* (Zarebanadkouki et al. 2016). Also, because neutrons are very sensitive to water, the application of neuron tomography to soil-root interactions was limited to 2D radiographic images (Carminati et al. 2010).

The putative role of the rhizosphere in regulating water uptake by changing its hydraulic properties has been well established (Bengough 2012), but the impact of abiotic stresses on this change is an issue that remains elusive. This paper aims to study this using maize in a pot-based microcosm. Two weeks after seedling emergence, healthy plants were subjected to water and salinity stresses, both in isolation and combination, of the kind typically encountered in important maize-growing aridic regions in the world. After an additional two weeks, we extracted the roots out to harvest the aggregates adhering to the roots and scanned them using X-ray CT. The porosity, pore-size distribution of all aggregates were estimated from the segmented images, while their permeability and tortuosity were calculated from pore-scale simulations of water flow and solute diffusion in the void space. Comparisons were made with aggregates taken from the unstressed control.

2. Materials and methods

2.1. Plant and soil

Maize (*Zea mays* L. var. Delprim) was grown in pots (20 cm high with an internal diameter of 15 cm) packed with a loamy sand soil collected from Woburn at Bedfordshire in the UK at a bulk density of 1.45g cm^{-3}. The soil was an Arenosol (FAO soil classification) comprising 80% sand, 12% silt and 8% clay (Nicholson et al. 2018). Prior to packing, the soil was firstly air-dried and then sieved (4 mm). The soil moisture in all pots was adjusted to 24% (weight content) before sowing the seeds at a depth of 5cm. The pots were then placed in a greenhouse at 25□ under 14h photoperiod (06:00-20:00) and irrigated with Hoagland nutrient solution at 3, 7 and 11 days after the seedling emergence respectively (three days after sowing). After the seedlings were established (two weeks after their emergence), we subjected some plants to water stress and salinity stress, in both isolation and combination, whilst a subset of the plants remained as unstressed controls (CK). We therefore created four treatments: CK (unstressed), water-stressed, salinity-stressed and water + salinity-stressed. Soil moisture in each pot was monitored using a WET-2 sensor connected to a HH2 meter (Delta-T120 Devices, UK). The water stress and salinity were to mimic what the maize grown in northern China often meets (Zhao et al. 2019). The CK treatment added 190 ml of Hoagland solution to the pot whenever the soil moisture measured using the sensor dropped to 60% of the field capacity (equivalent to 28%, weight content) and the water-stress irrigation treatment added 90 ml of Hoagland solution to the pots at the same time as the CK treatment. For the salinity stress associated with each irrigation treatment, 50mM of NaCl was added to the Hoagland solution in the first irrigation event, 14 days after the seedling emergence. Two weeks after the stresses started, we upturned each pot and gently removed the soil and roots out. The loose soil was shaken off the roots first and we then manually removed three aggregates adhering to different roots from each treatment. As a comparison we also took aggregates from an unplanted pot. All aggregates were geometrically irregular and their size was approximately in the range of 2-5 mm.

2.2. Image acquisition and processing

All aggregate samples were scanned using a Phoenix Nanotom X-ray CT scanner at the Hounsfield Facility at the University of Nottingham. The samples were loaded in a plastic tube which was mounted on the manipulation stage in the chamber of the scanner. The samples were scanned using an electron acceleration energy of 85 keV and a current of 100 μA at a spatial resolution of 4μm, with each sample taking approximately 30 mins to scan. Each scan consisted of the collection of 3600 images with a detector timing of 500 ms. The raw images were constructed using the software phoenix datos|x (Waygate Technologies) and they were then saved as a stack comprising 16-bit greyscale 2D slices.

The images were processed with Image J (University of Wisconsin-Madison). We first cropped the irregular images to a cube or cuboid prior to enhancing their contrast to 0.3% and converting the16-bit images to 8-bit images. The noise in the image was reduced before segmentation. A voxel was defined as a noisy voxel if its attenuation number differed markedly from those of its immediate adjacent voxels, and we replaced it by the average attenuation number of the adjacent voxels. The image was segmented using a threshold calculated from the IJ-IsoData algorithm in Image J.

Pore-size distribution in each image was calculated using the Plug-in CT-image Analysis & Manipulation (SCAMP) in Image J (Houston et al. 2017). To verify the method, we recalculated the pore-size distribution using Bone J finding the difference between the two was less than 5%. In what follows we only present the results obtained from SCAMP. Since all noisy voxels had been removed, only pores > 4μm were accounted in pore size calculation. We expressed pore-size distribution as relative volume of all pores with the same diameters rather than their absolute volume (Vogel and Kretzschmar 1996; Vogel et al. 2010).

Water and solute can only move through the pores that are hydraulically connected, and we thus removed the isolated pores using the method we previously proposed (Zhang et al. 2016b) before simulating water flow and solute diffusion. In what follows the porosity refers to the relative volume of all hydraulically connected pores.

2.3. Permeability

The permeability of each aggregate was calculated from pore-scale simulation of water flow using the lattice Boltzmann (LB) method we previously developed (Li et al. 2018a; Zhang et al. 2016b; Zhang et al. 2005; Zhang and Lv 2007) as given in the appendix. Water flow through the pore space was driven by an externally imposed pressure gradient. The flow was simulated to steady state when the absolute relative difference between the velocity in all voxels simulated at two times spanned 100 time steps was less than 10^{-7}. At steady state, the water velocity and water pressure in the voxels were volumetrically averaged over each section normal to the pressure gradient direction. The permeability of each aggregate was calculated as follows assuming that the volumetric average flow rate (q) and volumetric average pressure (P) follows the Darcy's law:

$$q = -\frac{k}{u}\nabla P, \qquad (1)$$

where k is the permeability and u is the dynamic viscosity of the water. The permeability of each aggregate was therefore be calculated as follows from the simulated results:

$$k = \frac{\mu q L}{P_0 - P_1}, \qquad (2)$$

where L is the length of the image in the direction over which the external pressure gradient was imposed, and P_0 and P_1 ($P_0 > P_1$) were the two constant pressures imposed on the two opposite sides of the image to drive the water to flow. For each cuboid image, we calculated its permeability in three directions. When imposing the pressure gradient in the z direction to calculate the permeability in this direction, q was calculated from

$$q = \frac{1}{N}\sum_{i=1}^{N} u_z\left(x_i, y_i, z_i\right), \tag{3}$$

where N is the number of all voxels in the image, $u_z(x_i, y_i, z_i)$ is the water velocity component at voxel centred on (x_i, y_i, z_i) and in the z direction. Permeability in other two directions was calculated similarly.

Once the permeability was known, its associated hydraulic conductivity K can be calculated from $K = kg / \upsilon_w$ where g is the gravitational acceleration and υ_w is the kinematic viscosity of the water. Since water viscosity is not a constant but varies with its chemical composition and temperature, in what follows we will use permeability rather than converting it to hydraulic conductivity.

2.4. Tortuosity

The permeability of a soil depends not only on its porosity but also on how the pores of different sizes are spatially connected. We used tortuosity to represent the change in pore connectedness in each aggregate and calculated it as the ratio between the effective diffusion coefficient of the aggregate for a solute and the bulk diffusion coefficient of the solute in free water. The effective diffusion coefficient was calculated using the lattice Boltzmann model we developed previously for pore-scale simulation as detailed in the appendix (Hu et al. 2014; Li et al. 2018b; Zhang et al. 2016a). As for the permeability, for each cuboid image we also calculated its tortuosity in the three directions.

2.5.

Statistical analysis

Statistical comparison of porosity, permeability, tortuosity and pore-size distribution between the treatments was performed using the software Matlab. The difference in the mean between the treatments was assessed by analysis of variance (ANOVA) and post-hoc pairwise comparisons of the treatment-means were performed using the Duncan's multiple range test with the difference considered significant at $p < 0.05$. The difference in pore-size distribution between the treatments was calculated using the Kolmogorov-Smimov test.

3. Results

Figure 1 shows four pairs of 3D greyscale images and their associated segmentations with one pair illustratively representing one treatment. Figure 2 compares a 2D slice and its segmentation. Visual comparison of the greyscale and segmented images in both 2D and 3D revealed that the segmentation method correctly captured the pore geometries.

Figure 3 compares the average pore-size distributions. In general, abiotic stress reduced the relative volume of large pores and increased the relative volume of small pores, especially for aggregates subjected to the combined salinity and water stress. Pore-size distributions for aggregates subjected to water and salinity stress in isolation are comparable and the Kolmogorov-Smimov test did not find significant difference between CK and all treatments. Because of beamtime limitation we only scanned one sample taken from the unplanted pot and thus excluded it in statistical analysis hereafter, and its porosity and permeability are shown the permeability section.

Figure 4a compares the porosity of the aggregates under different treatments. Abiotic stress led to a reduction in aggregate porosity, especially for the combined water and salinity stress which reduced the porosity significantly ($p<0.05$) from 0.246 in the CK to 0.167.

Difference between the three stress treatments, as well as the difference between the CK and the treatments with the stresses working in isolation, were not significant.

The tortuosity for different treatments was compared in Figure 4b. Abiotic stress resulted in a significant increase in tortuosity, compared with CK ($p<0.05$). There was no significant difference between the three stress treatments.

The permeability calculated for the three orthogonal directions in each aggregate differed for some aggregates. As permeability is a sensor, for the pressure gradient imposed in each direction we calculated both the diagonal and the off-diagonal permeability components and found that for most aggregates, the two off-diagonal permeability components were at least one order in magnitude smaller than the diagonal permeability components. In the analysis, we thus used the average of the three main permeability components in each aggregate to compare the treatments. Figure 4c shows the permeability of the aggregates under different treatments. It was manifested that both stresses reduced the rhizospheric permeability significantly ($p<0.05$) either working alone or in combination. Compared with the CK, water stress reduced the average permeability by approximately 60% and salinity stress by 80%, while combining water and salinity stress reduced the permeability by nearly 90% from 4.32 μm^2 to 0.49 μm^2. The reduction in permeability under stress is partly due to the decrease in porosity, and the relationship between the permeability and the porosity for all treatments appeared to follow a power law with an exponent of 4.42 as shown in Figure 5. However, the deviation from the power law indicates that the change in porosity was important but not the only reason.

4. Discussion

The permeability and tortuosity calculated from pore-scale simulations for aggregates not subjected to abiotic stress differed significantly from those subjected to water and salinity stresses, although the differences between the treatments with the stresses working alone or in combination were not statistically significant (Figures 4b, c). As we thoroughly sieved and mixed the soil before packing it into the pots, the aggregates formed on the root surfaces were likely the consequence of roots and root-mediated processes. As such, the variation between their permeability and tortuosity was due to the impact of the treatments rather than spatial heterogeneity. This was also corroborated by the porosity, for which we found significant difference ($p<0.05$) only between the CK and the treatment with combined water and salinity stresses, while the differences between the CK and other treatments were not significant (Figure 4a). These results alluded that the change in permeability and tortuosity was not solely caused by porosity change, and that the pore structure formed by biotic activities in the aggregates, such as root hairs and fungus, might also play an important role. These, along with other processes, made the aggregates in the vicinity of the rhizosphere respond differently to the abiotic stresses (Crawford et al. 2012), although it was impossible to discern the relative dominance of one over another.

Compared to the CK, salinity working in isolation or combined with water stress reduced the permeability and tortuosity of the aggregates at $p<0.05$ significant level (Figures 4b, c). NaCl was added to deliberately salinize the soil and the Na could have dispersed the clay particles and consequently weakened the aggregation in both the rhizosphere and bulk soil. This could be one reason underlying the reduced porosity and permeability of the rhizosphere under salinity stress, but this does not appear to be the only one as water stress also reduced porosity as much as the salinity did (Figure 4a).

Soil permeability depends not only on porosity but also on how pores of different sizes are spatially organized. The tortuosity of aggregates under different treatments showed that salinity rendered the soil more tortuous than water stress, making the aggregate more difficult for water and solute to move (Figures 4b). Although salinity and water stress changed intra-aggregates pores and their ability to transport water and solute, the change in permeability with porosity for samples taken from all treatments appears to follow the common relationship (R^2=0.65) as shown in Figure 5, manifesting the importance of porosity. However, the deviation from the power law implies that the shape and spatial organization of the pores also played an important role.

Reduction in rhizosphere porosity and its ability to conduct water and solute due to water and salinity stresses would restrict root uptake of water and acquisition of dissolved solutes by the plant. Apparently, we do not know if this is a physiological response of the plant as a self-defence mechanism to reduce transpiration (saving water under water stress) and salt uptake (ameliorating salt toxicity) or purely a passive soil physical process without active involvement of the plant.

Visual observation of the root architectures revealed that the abiotic stresses curtailed root ramifying and made the roots thinner than those not under stress (Figure 6). Radial expansion of roots locally compacts the soil and thus thick roots should mechanically densify the rhizosphere more than the thin roots. However, our data do not support this and in contrast, the opposite appears to be true indicating that other mechanisms might have played a role in structural and hydraulic change in the rhizosphere under water and salinity stresses.

Maize is known to exude a large amount of mucilage into the soil providing C to support a diverse microbial community. This process can bind soil particles together and enhance aggregation in the rhizosphere (Benard et al. 2019). Aggregates bound by mucilage are quite stable even after desiccation (Benard et al. 2019); such aggregations could create pores detectable by X-ray imaging at resolution of 4μm. For example, the experimental study of Benard et al (2019) showed that amending soil with maize mucilage increased soil porosity by 10% but reduced the hydraulic conductivity because of the increase in water viscosity. We speculated that the abiotic stress might alter mucilage secretion and change soil aggregation and the intra-aggregate structure as a result. We used permeability rather than hydraulic conductivity to describe the ability of the aggregates to conduct fluid as we do not know to what extent the abiotic stresses and root-mediated processes had altered the water viscosity. In addition to mucilage, the difference in root hair proliferation under different treatments could be another mechanism underlying the change in porosity and permeability as affected by abiotic stresses (Rabbi et al. 2018).

The enhanced aggregation by roots and their associated abiotic and biotic activities also create large pores between the aggregates. Due to technical limitations, it was not possible to scan the entire pots (20 cm high and 15 cm in diameter) at a resolution high enough to identify the inter-aggregate pores. Therefore, our results on the impact of abiotic stresses on soil structure were limited to the aggregates adhering to the roots rather than the alteration in properties of the whole soil that includes both inter-aggregate and intra-aggregate features. Also, we repacked soil into pots and conducted the experiments in a controlled environment. This limited the space for roots to grow and did not capture the physical and biochemical heterogeneity of the soil. Therefore, in is prudent not extrapolate our findings to those of maize growing in field conditions. Notwithstanding these, our results do shed some light on the role of abiotic stresses in mediating root-soil interactions and provide a way in which we may improve our mechanistic understanding of the impact of real-world abiotic stresses on crop growth.

5. Conclusions

This paper studied the impact of abiotic stresses on structural change in the rhizosphere of maize and its consequence for the rhizospheric permeability and tortuosity using X-ray CT and pore-scale simulations. The results showed that compared to an unstressed control, water stress reduced the soil permeability by approximately 60% and the salinity stress reduced this by 80% when working in isolation, while the two stresses in combination reduced the soil permeability by 90%. Since water and nutrients need to pass through the rhizosphere before being taken up by roots, change in hydraulic properties in the rhizosphere has important implications for unravelling how roots respond to abiotic stress. Given the increased interest in improving crop productivity by manipulating their root traits, understanding the changes in hydraulic properties of the rhizosphere in response to abiotic stresses is critical. Since the rhizosphere is only a few millimetres around the root and directly measuring its hydraulic conductivity is difficult technically, combining pore-scale simulation and X-ray CT, as described in this paper, could help to bridge this gap.

Appendix A

Water flow and solute diffusion through the void space of the segmented images were both simulated by the following lattice Boltzmann model (d'Humieres et al. 2002):

$$f_i\left(\boldsymbol{x}+\delta t\boldsymbol{e}_i, t+\delta t\right)=f_i\left(\boldsymbol{x},t\right)+M^{-1}SM\left[f_i^{eq}\left(\boldsymbol{x},t\right)-f_i\left(\boldsymbol{x},t\right)\right], \qquad \text{(A1)}$$

where $f_i\left(\boldsymbol{x},t\right)$ is the particle distribution function at location $\boldsymbol{x}$ and time t moving at lattice velocity $\boldsymbol{e}_i$, δx is the size of the image voxels, δt is a time step, $f_i^{eq}\left(\boldsymbol{x},t\right)$ is the equilibrium distribution function, M is a transform matrix and S is the collision matrix. The models for water flow and solute transport differed only in their equilibrium distribution functions, both involving a collision step and a streaming step to advance a time step. In each model, the collision was calcculed as $m=SM\left[f_i^{eq}\left(\boldsymbol{x},t\right)-f_i\left(\boldsymbol{x},t\right)\right]$ first and m was then then transformed back to particle distribution functions by $M^{-1}m$. In both models, we used the D3Q19 lattice in which the particles move in 19 directions with velocities: $\left(0,\ 0,\ 0\right)$, $\left(\pm\delta x/\delta t,\ \pm\delta x/\delta t,\ 0\right)$, $\left(0,\ \pm\delta x/\delta t,\ \pm\delta x/\delta t\right)$, $\left(\pm\delta x/\delta t,\ 0,\ \pm\delta x/\delta t\right)$ and $\left(\pm\delta x/\delta t,\ \pm\delta x/\delta t,\ \pm\delta x/\delta t\right)$ (Qian et al. 1992).

Model for water flow

The collision matrix in the model for water flow is diagonal:

$$\begin{aligned}
&S = \left(s_0, s_1, s_2, s_3, s_4, s_5, s_6, s_7, s_8, s_9, s_{10}, s_{11}, s_{12}, s_{13}, s_{14}, s_{15}, s_{16}, s_{17}, s_{18}\right)^T, \\
&s_0 = s_3 = s_5 = s_7 = 0, \\
&s_1 = s_2 = s_{9-15} = 1/\tau, \\
&s_4 = s_6 = s_8 = s_{16-18} = 8(2-\tau^{-1})/(8-\tau^{-1}),
\end{aligned} \tag{A2}$$

and the equilibrium distribution functions are

$$\begin{aligned}
&f_i^{eq} = w_i \left[\rho + \rho_0 \left(\frac{3\boldsymbol{e}_i \cdot \boldsymbol{u}}{s^2} + \frac{9\left(\boldsymbol{e}_i \cdot \boldsymbol{u}\right)^2}{2s^4} - \frac{3\boldsymbol{u} \cdot \boldsymbol{u}}{2s^2} \right) \right], \\
&w_0 = 1/3, \\
&w_i = 1/18, \qquad \left\|\boldsymbol{e_i}\right\| = \delta x / \delta t \\
&w_i = 1/36 \qquad \left\|\boldsymbol{e_i}\right\| = \sqrt{2}\delta x / \delta t
\end{aligned} \tag{A3}$$

where $s = \delta x / \delta t$ and ρ_0 is a reference fluid density to ensure an incompressible fluid at steady state (Zou et al. 1995). The water density ρ and bulk water velocity $\boldsymbol{u}$ are calculated from

$$\begin{aligned}
&\rho = \sum_{i=0}^{18} f_i, \\
&\boldsymbol{u} = \sum_{i=1}^{18} f_i \boldsymbol{e}_i / \rho_0.
\end{aligned} \tag{A4}$$

The kinematic viscosity of fluid was $\nu = \delta x^2(\tau - 0.5)/6\delta t$ and its pressure is related to density in $p = \rho\delta x^2 / 3\delta t^2$.

Model for solute diffusion

The equilibrium distribution functions for solute diffusion are defined by

$$f_i^{eq} = w_i c, \tag{A5}$$

where *c* is solute concentration and the weighting parameter w_i is the same as those defined in Eq. (A3). The diagonal collision matrix for solute diffusion is uniform:

$$S = \left(\tau_0, \tau_0, \tau_0, \tau_0, \tau_0, \tau_0, \tau_0, \tau_0, \tau_0, \tau_0, \tau_0, \tau_0, \tau_0, \tau_0, \tau_0, \tau_0, \tau_0, \tau_0, \tau_0\right)^T, \tag{A6}$$

The collision can thus be directly calculated from $m = \tau_0\left[f_i^{eq}\left(\boldsymbol{x},t\right) - f_i\left(\boldsymbol{x},t\right)\right]$ without need of the transform as for fluid flow. The concentration *c* and the diffusice flux $\boldsymbol{j}$ in each voxel are calculated from

$$\begin{aligned} c &= \sum\nolimits_{i=0}^{18} f_i^{eq}, \\ \boldsymbol{j} &= \sum\nolimits_{i=0}^{18} (1 - 0.5/\tau_0) e_i f_i^{eq}, \end{aligned} \tag{A7}$$

The mollecular diffusion coefficient in the above model is $D_0 = \delta x^2 (1/\tau_0 - 0.5)/6\delta t$. The effective diffusion coefficient of the image was calculated using the method proposed in our previous work (Zhang et al. 2016a).

Model implementation

For both water flow and solute diffusion, there are two calculations to advance one time step. The first one is to calculate the collisions: $f_i^* = f_i(\boldsymbol{x},t) + M^{-1}SM\left[f_i^{eq}(\boldsymbol{x},t) - f_i(\boldsymbol{x},t)\right]$ for water and $f_i^* = f_i(\boldsymbol{x},t) + \tau_0\left[f_i^{eq}(\boldsymbol{x},t) - f_i(\boldsymbol{x},t)\right]$ for solute, and the second step is to move f_i^* to $\boldsymbol{x} + \delta t\boldsymbol{e}_i$ at the end of δt. Whenever f_i^* hits a solid voxel during the streaming, it is bounced back to where it emanates to ensure a zero velocity on the water-solid interface for both water flow and solute diffusion.

Acknowledgements

YG was supported by the National Natural Science Foundation of China (NSFC51790534, 51879267). The work at Rothamsted Research is part of the soil to nutrition (S2N) strategic programme (BBS/E/C/000I0310, 2017-2022) funded by the Biotechnology and Biological Sciences Research Council (BBSRC) of the UK. This work also formed part of the Joint UK-China Centre for the Sustainable Intensification of Agriculture project funded by BBSRC through the Newton Fund (BBS/OS/NW/000004, 2015-2019).

References

Ahmed MA, Zarebanadkouki M, Ahmadi K, Kroener E, Kostka S, Kaestner A, Carminati A (2018) Engineering Rhizosphere Hydraulics: Pathways to Improve Plant Adaptation to Drought. Vadose Zone J 17: 12. doi: 10.2136/vzj2016.09.0090.

Alami Y, Achouak W, Marol C, Heulin T (2000) Rhizosphere soil aggregation and plant growth promotion of sunflowers by an exopolysaccharide-producing Rhizobium sp strain isolated from sunflower roots. Appl Environ Microbiol 66: 3393-3398. doi: 10.1128/aem.66.8.3393-3398.2000.

Benard P, Zarebanadkouki M, Brax M, Kaltenbach R, Jerjen I, Marone F, Couradeau E, Felde V, Kaestner A, Carminati A (2019) Microhydrological Niches in Soils: How Mucilage and EPS Alter the Biophysical Properties of the Rhizosphere and Other Biological Hotspots. Vadose Zone J 18: 10. doi: 10.2136/vzj2018.12.0211.

Bengough AG (2012) Water Dynamics of the Root Zone: Rhizosphere Biophysics and Its Control on Soil Hydrology. Vadose Zone J 11: 6. doi: 10.2136/vzj2011.0111.

Carminati A (2012) A Model of Root Water Uptake Coupled with Rhizosphere Dynamics. Vadose Zone J 11: 9. doi: 10.2136/vzj2011.0106.

Carminati A (2013) Rhizosphere wettability decreases with root age: a problem or a strategy to increase water uptake of young roots? Front Plant Sci 4: 9. doi: 10.3389/fpls.2013.00298.

Carminati A, Moradi AB, Vetterlein D, Vontobel P, Lehmann E, Weller U, Vogel HJ, Oswald SE (2010) Dynamics of soil water content in the rhizosphere. Plant Soil 332: 163-176. doi: 10.1007/s11104-010-0283-8.

Carminati A, Schneider CL, Moradi AB, Zarebanadkouki M, Vetterlein D, Vogel HJ, Hildebrandt A, Weller U, Schuler L, Oswald SE (2011) How the Rhizosphere May Favor Water Availability to Roots. Vadose Zone J 10: 988-998. doi: 10.2136/vzj2010.0113.

Crawford JW, Deacon L, Grinev D, Harris JA, Ritz K, Singh BK, Young I (2012) Microbial diversity affects self-organization of the soil-microbe system with consequences for function. J R Soc Interface 9: 1302-1310. doi: 10.1098/rsif.2011.0679.

d'Humieres D, Ginzburg I, Krafczyk M, Lallemand P, Luo LS (2002) Multiple-relaxation-time lattice Boltzmann models in three dimensions. Philos Trans R Soc Lond Ser A-Math Phys Eng Sci 360: 437-451. doi: 10.1098/rsta.2001.0955.

Daly KR, Mooney SJ, Bennett MJ, Crout NMJ, Roose T, Tracy SR (2015) Assessing the influence of the rhizosphere on soil hydraulic properties using X-ray computed tomography and numerical modelling. J Exp Bot 66: 2305-2314. doi: 10.1093/jxb/eru509.

Dexter AR (1987) Compression of soil around roots Plant Soil 97: 401-406. doi: 10.1007/bf02383230.

Gregory PJ (2006) Roots, rhizosphere and soil: the route to a better understanding of soil science? Eur J Soil Sci 57: 2-12. doi: 10.1111/j.1365-2389.2005.00778.x.

Hallett PD, Gordon DC, Bengough AG (2003) Plant influence on rhizosphere hydraulic properties: direct measurements using a miniaturized infiltrometer. New Phytol 157: 597-603. doi: 10.1046/j.1469-8137.2003.00690.x.

Helliwell JR, Sturrock CJ, Miller AJ, Whalley WR, Mooney SJ (2019) The role of plant species and soil condition in the structural development of the rhizosphere. Plant Cell Environ 42: 1974-1986. doi: 10.1111/pce.13529.

Hinsinger P, Bengough AG, Vetterlein D, Young IM (2009) Rhizosphere: biophysics, biogeochemistry and ecological relevance. Plant Soil 321: 117-152. doi: 10.1007/s11104-008-9885-9.

Hinsinger P, Gobran GR, Gregory PJ, Wenzel WW (2005) Rhizosphere geometry and heterogeneity arising from root-mediated physical and chemical processes. New Phytol 168: 293-303. doi: 10.1111/j.1469-8137.2005.01512.x.

Houston AN, Otten W, Falconer R, Monga O, Baveye PC, Hapca SM (2017) Quantification of the pore size distribution of soils: Assessment of existing software using tomographic and synthetic 3D images. Geoderma 299: 73-82. doi: 10.1016/j.geoderma.2017.03.025.

Hu WL, Huang N, Zhang XX (2014) Impact of saturation on mass transfer rate between mobile and immobile waters in solute transport within aggregated soils. J Hydrol 519: 3557-3565. doi: 10.1016/j.jhydrol.2014.10.057.

Huang YJ, Yang ZJ, Ren WY, Liu GH, Zhang CZ (2015) 3D meso-scale fracture modelling and validation of concrete based on in-situ X-ray Computed Tomography images using damage plasticity model. Int J Solids Struct 67-68: 340-352. doi: 10.1016/j.ijsolstr.2015.05.002.

Kroener E, Zarebanadkouki M, Kaestner A, Carminati A (2014) Nonequilibrium water dynamics in the rhizosphere: How mucilage affects water flow in soils. Water Resour Res 50: 6479-6495. doi: 10.1002/2013wr014756.

Li ZY, Wang D, Zhang XX, Crawford JW (2018a) Water flow across the interface of contrasting materials: Pressure discontinuity and its implications. J Hydrol 566: 435-440. doi: 10.1016/j.jhydrol.2018.09.029.

Li ZY, Zhang XX, Wang D, Liu Y (2018b) Direct methods to calculate the mass exchange between solutes inside and outside aggregates in macroscopic model for solute transport in aggregated soil. Geoderma 320: 126-135. doi: 10.1016/j.geoderma.2018.01.021.

Nicholson F, Bhogal A, Taylor M, McGrath S, Withers P (2018) Long-term Effects of Biosolids on Soil Quality and Fertility. Soil Sci 183: 89-98. doi: 10.1097/ss.0000000000000239.

Qian YH, Dhumieres D, Lallemand P (1992) Lattice BGK models for Navier-Stokes equation. Europhysics Letters 17: 479-484. doi: 10.1209/0295-5075/17/6/001.

Rabbi SMF, Tighe MK, Flavel RJ, Kaiser BN, Guppy CN, Zhang XX, Young IM (2018) Plant roots redesign the rhizosphere to alter the three-dimensional physical architecture and water dynamics. New Phytol 219: 542-550. doi: 10.1111/nph.15213.

Read DB, Bengough AG, Gregory PJ, Crawford JW, Robinson D, Scrimgeour CM, Young IM, Zhang K, Zhang X (2003) Plant roots release phospholipid surfactants that modify the physical and chemical properties of soil. New Phytol 157: 315-326. doi: 10.1046/j.1469-8137.2003.00665.x.

Read DB, Gregory PJ (1997) Surface tension and viscosity of axenic maize and lupin root mucilages. New Phytol 137: 623-628. doi: 10.1046/j.1469-8137.1997.00859.x.

Ren WY, Yang ZJ, Sharma R, Zhang C, Withers PJ (2015) Two-dimensional X-ray CT image based meso-scale fracture modelling of concrete. Eng Fract Mech 133: 24-39. doi: 10.1016/j.engfracmech.2014.10.016.

Schwartz N, Carminati A, Javaux M (2016) The impact of mucilage on root water uptake-A numerical study. Water Resour Res 52: 264-277. doi: 10.1002/2015wr018150.

Totzke C, Kardjilov N, Manke I, Oswald SE (2017) Capturing 3D Water Flow in Rooted Soil by Ultra-fast Neutron Tomography. Sci Rep 7: 9. doi: 10.1038/s41598-017-06046-w.

Tracy SR, Daly KR, Sturrock CJ, Crout NMJ, Mooney SJ, Roose T (2015) Three-dimensional quantification of soil hydraulic properties using X-ray Computed Tomography and image-based modeling. Water Resour Res 51: 1006-1022. doi: 10.1002/2014wr016020.

Vogel HJ, Kretzschmar A (1996) Topological characterization of pore space in soil — sample preparation and digital image-processing. Geoderma 73: 23-38. doi: https://doi.org/10.1016/0016-7061(96)00043-2.

Vogel HJ, Weller U, Schlüter S (2010) Quantification of soil structure based on Minkowski functions. Computers & Geosciences 36: 1236-1245. doi: 10.1016/j.cageo.2010.03.007.

Zarebanadkouki M, Ahmed MA, Carminati A (2016) Hydraulic conductivity of the root-soil interface of lupin in sandy soil after drying and rewetting. Plant Soil 398: 267-280. doi: 10.1007/s11104-015-2668-1.

Zhang XX, Crawford JW, Flavel RJ, Young IM (2016a) A multi-scale Lattice Boltzmann model for simulating solute transport in 3D X-ray micro-tomography images of aggregated porous materials. J Hydrol 541: 1020-1029. doi: 10.1016/j.jhydro1.2016.08.013.

Zhang XX, Crawford JW, Young IM (2016b) A Lattice Boltzmann model for simulating water flow at pore scale in unsaturated soils. J Hydrol 538: 152-160. doi: 10.1016/j.jhydrol.2016.04.013.

Zhang XX, Deeks LK, Bengough AG, Crawford JW, Young LM (2005) Determination of soil hydraulic conductivity with the lattice Boltzmann method and soil thin-section technique. J Hydrol 306: 59-70. doi: 10.1016/j.jhydrol.2004.08.039.

Zhang XX, Fan XY, Li ZY (2016c) Water velocity at water-air interface is not zero: Comment on "Three-dimensional quantification of soil hydraulic properties using X-ray computed tomography and image-based modeling" by Saoirse R. Tracy et al. Water Resour Res 52: 5687-5690. doi: 10.1002/2015wr018432.

Zhang XX, Lv MC (2007) Persistence of anomalous dispersion in uniform porous media demonstrated by pore-scale simulations. Water Resour Res 43: 11. doi: 10.1029/2006wr005557.

Zhao B, Wang XL, Ata-Ul-Karim ST, Liu ZD, Duan AW (2019) Effect of Straw Incorporation on Corn Yield in North China: A Meta-Analysis. J Biobased Mater Bioenergy 13: 532-536. doi: 10.1166/jbmb.2019.1872.

Zou QS, Hou SL, Chen SY, Doolen GD (1995) An improved incompressible Lattice Boltzmann model for time-independent flows. . Journal of Statistical Physics 81: 35-48. doi: 10.1007/bf02179966.

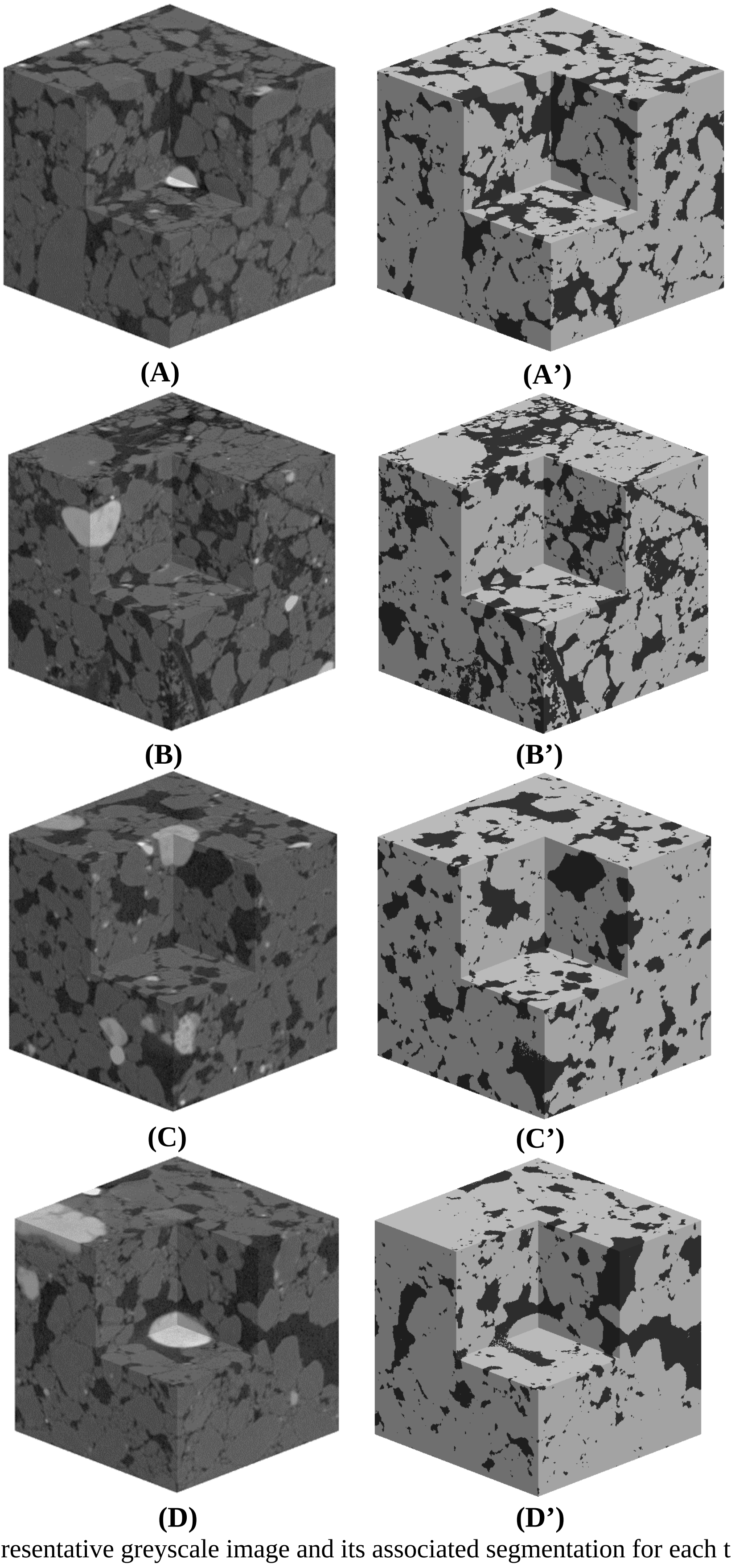
(A) (A')

(B) (B')

(C) (C')

(D) (D')

FIGURE 1. Representative greyscale image and its associated segmentation for each treatment acquired using the X-ray CT at resolution of 4 um. A-A: unstressed control; B-B': water stress; C-C: salinity stress; D-D': combined water and salinity stresses. Pores are in black and solids are in grey.

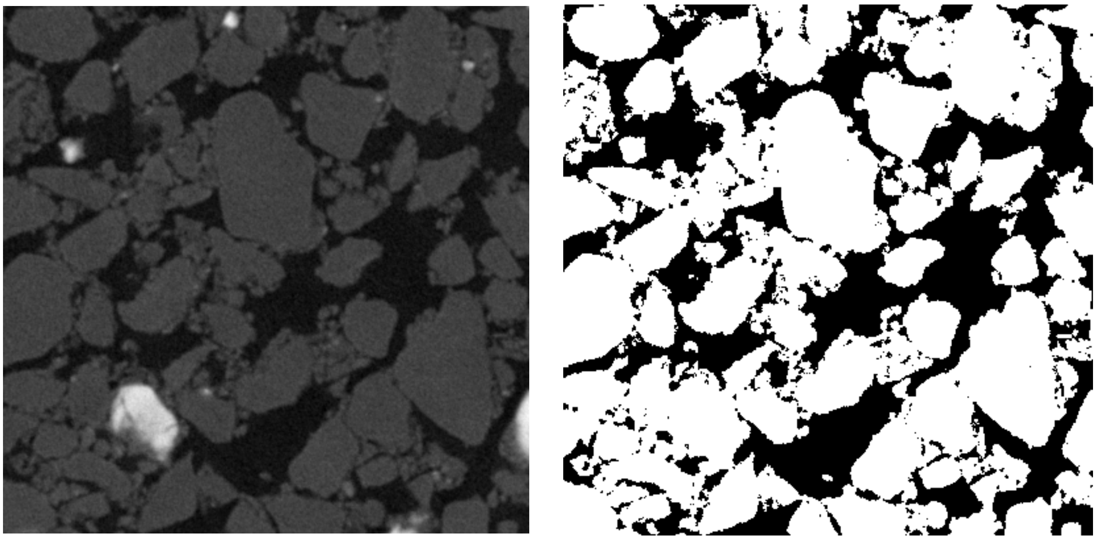

FIGURE 2. Schematic comparison of a greyscale 2D slice and its segmentation.

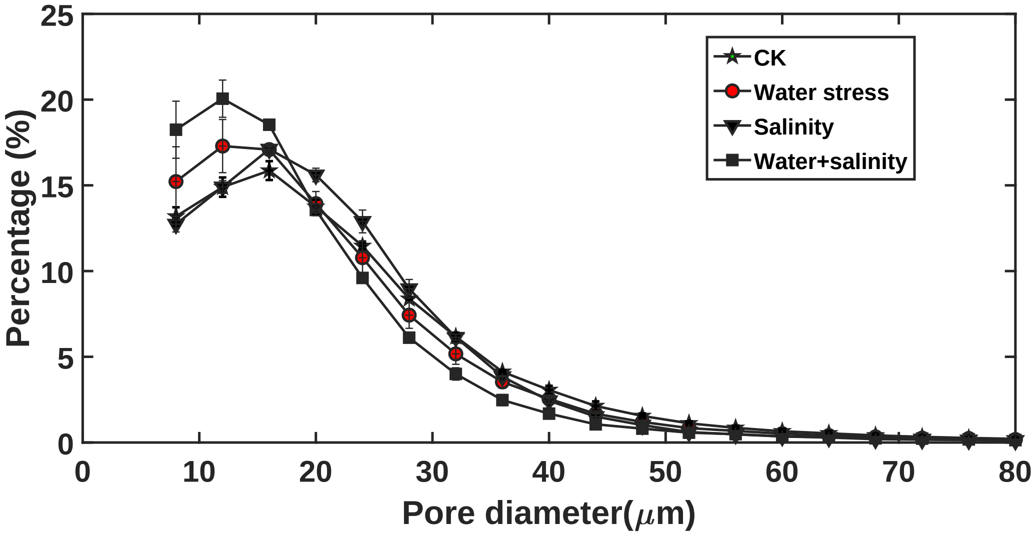

FIGURE 3. Comparison of pore-size distributions for aggregates taken from different abiotic stress treatments and the unstressed control (CK).

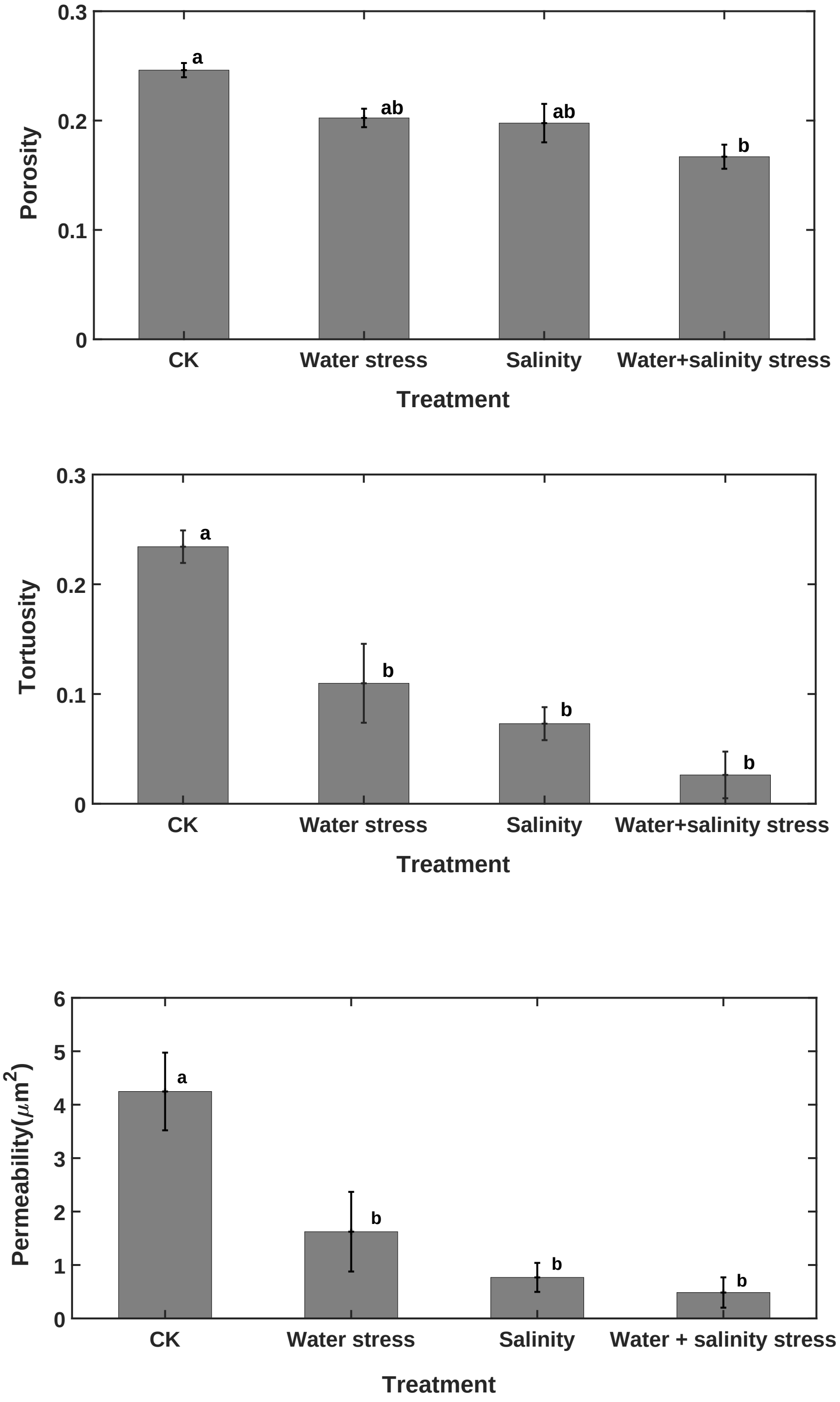

FIGURE 4. Comparison of the porosity (A), tortuosity (B) and permeability (C) of the aggregates taken from different stress treatments and the unstressed control (CK). The lowercase letters on top of the bars represent significant difference at $p<0.05$.

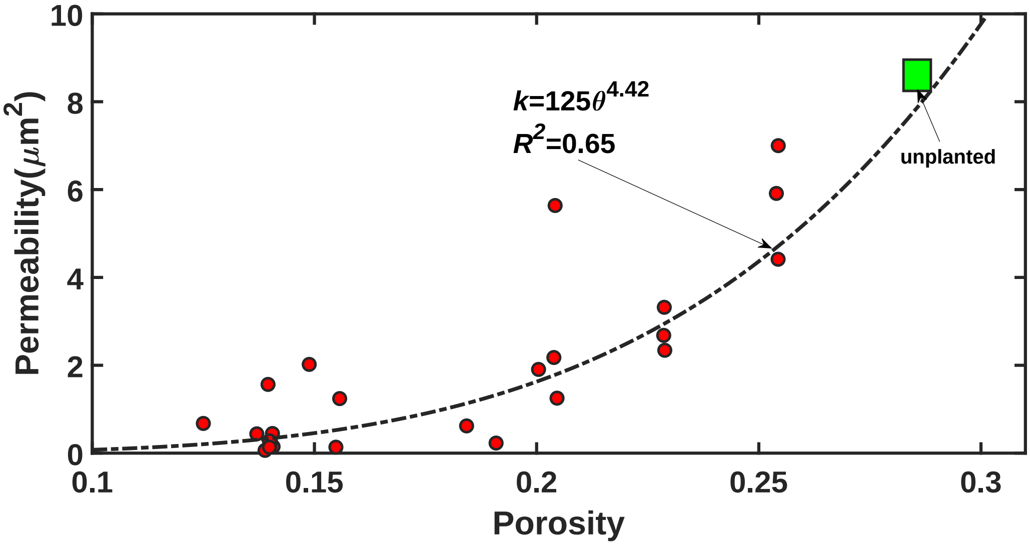

FIGURE 5. Change in permeability (symbols) with porosity θ for all aggregates taken from all treatments, and the fitting of power-law k=125 $\theta^{4.42}$ (solid line). The result for the unplanted sample is also plotted.

FIGURE 6. Illustrative examples showing the impact of stress on root growth: A: unstressed CK; B: salinity stress.